

Synthesis of Nanoparticles by Electroless Deposition and/or Spark Generation and Their Applications

Jeong Hoon Byeon

The Graduate School
Yonsei University
Department of Mechanical Engineering

Synthesis of Nanoparticles by Electroless Deposition and/or Spark Generation and Their Applications

A Dissertation

Submitted to the Department of Mechanical Engineering
and the Graduate School of Yonsei University
in partial fulfillment of the
requirements for the degree of
Doctor of Philosophy in Mechanical Engineering

Jeong Hoon Byeon

December 2007

This certifies that the dissertation
of Jeong Hoon Byeon is approved.

Thesis Supervisor: [Jungho Hwang]

[Yong-Jun Kim: Thesis Committee Member #1]

[Hyo-II Jung: Thesis Committee Member #2]

[Chang-Ha Lee: Thesis Committee Member #3]

[Mansoo Choi: Thesis Committee Member #4]

The Graduate School
Yonsei University
December 2007

Dedicated to my family

Acknowledgement

At the point of finishing my Ph.D study, I would like to express my gratitude to many people. Without their support, help, advice, and friendship, the completion of my degree wouldn't have been possible.

First, I would like to thank my advisor, Prof. Jungho Hwang, for his invaluable guidance, encouragement, suggestion and patience throughout my graduate study at Yonsei University. He is always there whenever I turn to him with questions to which he is constantly full of solutions and advice. He has fostered such a working and research environment in this group that I feel I had the maximum degree of freedom to conduct my research based on my interest. He has coached me how to be a good researcher with insights and vision in the field, which is also highly appreciated.

I also owe my thanks to Prof. Mansoo Choi, Prof. Chang-Ha Lee, Prof. Yong-Jun Kim, and Prof. Hyo-Il Jung for their discussion and suggestions during my Ph.D study and their service on my Ph.D committee.

I would like to thanks to Jae Hong Park and Ki Young Yoon for the enjoyable time since we worked together in our laboaratory. It has been one of the most productive periods throughout my study. A lot of new ideas were generated from our discussions of out results after work everyday. That experience set my positive attitude towards collaborations among researchers.

I also would like to say "thank you" to other previous and present members, Byung Ju Ko, Chul Woo Park, Ryang Hwa Lee, Sang Yoon Kim, Yee Kyeong Jung, Dae Young Lee, Dongho Park, Dr. Jun-Ho Ji, and others for their help and friendship.

My deepest appreciations go to my parents and my brother. Their constant encouragement and unwavering support have always been a motivating force in my life. Their countless sacrifices make it possible for me to be where I am today.

Last, but not least, I would like to thank my wife, Hyo-Jin Lee, for her understanding and love during the past ten years. Her support, encouragement, and help have been a constant source for strength of me through this long journey of my dissertation study. My sweet baby, Seung Joo Byeon, her cute things also have been a constant source for strength of me.

Contents

List of Figures	vi
List of Tables	xii
Abstract	1
1. Nanoparticle synthesis by electroless deposition (ELD)	3
1.1 Introduction	3
1.1.1 ELD of copper (Cu) onto pitch-based activated carbon fibers (ACF)	3
1.1.2 ELDs of Cu and silver (Ag) onto rayon-based ACF	5
1.1.3 ELDs of Cu and Ag onto multiwall carbon nanotubes (MWNT)	7
1.2 Materials and methods	9
1.2.1 Preparations and characterizations of Cu deposited ACF and a test for NO removal	9

1.2.2 Preparations and characterizations of Cu and Ag deposited ACF and tests for antibacterial action and VOC adsorption-desorption	12
1.2.3 Preparations and characterizations of Cu and Ag deposited MWNT	16
1.3 Results and discussion	19
1.3.1 ELD of Cu onto pitch-based ACF and an application for NO removal	19
1.3.2 ELDs of Cu and Ag onto rayon-based ACF and applications for antibacterial action and VOC adsorption-desorption	26
1.3.3 Progresses of Cu and Ag ELDs onto MWNT	37
1.4 Summaries and conclusions	43
2. Nanoparticle synthesis by spark generation (SG)	45
2.1 Introduction	45
2.1.1 SGs of aerosol monometallic and bimetallic nanoparticles	45
2.1.2 SGs of aerosol carbon nanoparticles	46

2.1.3 SGs of aerosol carbon-encapsulated metal nanoparticles (CEMNs)	47
2.2 Materials and Methods	49
2.2.1 Preparations and characterizations of aerosol monometallic and bimetallic nanoparticles	49
2.2.2 Preparations and characterizations of aerosol carbon nanoparticles	51
2.2.3 Preparations and characterizations of aerosol CEMNs	53
2.3 Results and discussion	55
2.3.1 Properties and mechanisms of SGs aerosol monometallic and bimetallic nanoparticles	55
2.3.2 Textural properties and VOC removal of SG aerosol carbon nanoparticles	67
2.3.3 Properties and mechanisms of SGs aerosol CEMNs	70
2.4 Summaries and conclusions	75
3. Nanoparticle synthesis by combining of SG and ELD	77
3.1 Introduction	77

3.1.1 Catalytic surface activation via aerosol palladium (Pd) nanoparticles for use in Ag ELD onto ACF	77
3.1.2 Site-selective catalytic surface activation via aerosol Pd ELD onto flexible polyimide (FPI) substrate for use in Cu micropatterning	78
3.1.3 Site-selective catalytic surface activation via aerosol platinum (Pt) ELD onto FPI substrate for use in Ag micropatterning	80
3.2 Materials and Methods	81
3.2.1 Preparations and characterizations of Pd aerosol activation and Ag ELD onto ACF	81
3.2.2 Preparations and characterizations of site-selective Pd aerosol activation and Cu ELD onto FPI	84
3.2.3 Preparations and characterizations of site-selective Pt aerosol activation and Ag ELD onto FPI	88
3.3 Results and discussion	89
3.3.1 Properties of Pd aerosol activation and Ag ELD onto ACF	89

3.3.2 Properties of site-selective Pd aerosol activation and Cu micropatterining onto FPI	98
3.3.3 Properties of site-selective Pt aerosol activation and Ag micropatterining onto FPI	105
3.4 Summaries and conclusions	111
Supplementary data 1	112
Supplementary data 2	123
Supplementary data 3	128
Supplementary data 4	135
References	137
Abstract in Korean	149

List of Figures

- Figure 1. Diagram of the experimental setup for the NO removal test.
- Figure 2. Experimental set-up for tests of pressure drop and filtration.
- Figure 3. (a) Processes for silver metallization. (b) Schematic diagram of the microfiltration unit.
- Figure 4. FESEM micrographs of the pristine and copper deposited ACF.
- Figure 5. EDX profiles of the pristine and copper deposited ACF.
- Figure 6. X-ray diffraction patterns of the copper deposited ACF.
- Figure 7. Amount of copper as a function of the deposition time (by ICP-AES analysis).
- Figure 8. NO removal characteristics of the pristine and copper deposited ACF.
- Figure 9. Pore size distributions of the pristine and copper deposited ACF.
- Figure 10. Pore size distributions of the pristine and copper-deposited ACF.
- Figure 11. Steady-state NO removal vs amount of copper.
- Figure 12. SEM and ICP-AES results of the pristine and copper deposited ACF.
- Figure 13. X-ray diffraction patterns of the copper deposited ACF.
- Figure 14. Results for antibacterial tests.
- Figure 15. VOC adsorption and desorption characteristics of the pristine and the copper deposited ACF.
- Figure 16. SEM images of (a) Ag-00, (b) Ag-10, (c) Ag-20 and (d) Ag-30.
- Figure 17. Pressure drop of the ACF filters (Mean \pm SD).
- Figure 18. Filtration efficiency of the ACF discs (Mean \pm SD).
- Figure 19. Antimicrobial effects of the test discs on *E. coli* (Mean \pm SD).
- Figure 20. Antimicrobial effects of the test discs on *B. subtilis* (Mean \pm SD).

Figure 21. Morphological and chemical analyses of the MWNTs. (a) HRTEM image (scale bar, 20 nm) of the nitric acid-treated MWNTs. (b) HRTEM image (scale bar, 20 nm) of the Sn-Pd activated and accelerated MWNTs. (c) HRTEM image (scale bar, 20 nm) of the silver coated MWNTs (for 3 minutes). (d) HRTEM image (scale bar, 20 nm) of the silver coated MWNTs (for 5 minutes). (e) HRTEM image (scale bar, 20 nm) of the silver coated MWNTs (for 10 minutes). (f) Particle size distribution of silver particles on the MWNTs from the HRTEM image (scale bar, 5 nm). (g) EDX profile of the silver deposited MWNTs (for 5 minutes).

Figure 22. XRD patterns of the silver coated MWNTs.

Figure 23. Adsorption isotherms of the silver coated MWNTs.

Figure 24. Schematic setup of spark generation.

Figure 25. Experimental setup for tests of VOC adsorption-desorption.

Figure 26. Particle size distributions of monometallic nanoparticles.

Figure 27. Morphological, chemical, and structural results of Pd and Au monometallic nanoparticles. (a) SEM micrographs and EDX profiles. (b) TEM micrographs and SAED patterns.

Figure 28. X-ray diffractograms of monometallic nanoparticles.

Figure 29. Mechanism of spark generated monometallic nanoparticles.

Figure 30. Particle size distributions of bimetallic nanoparticles.

Figure 31. Morphological, chemical and structural results of Pd:Au bimetallic nanoparticles. (a) SEM micrograph and EDX profile. (b) TEM micrograph and SAED pattern.

Figure 32. X-ray diffractograms of bimetallic nanoparticles.

Figure 33. Mechanism of spark generated bimetallic nanoparticles.

Figure 34. Morphology and size distribution of generated carbon particles.

Figure 35. Pore size distribution of generated carbon particles.

Figure 36. Spark generated particles (anode: Ni, cathode: C). (a) TEM image with local EDX information of spark generated particles. Scale bar, 200nm. (b) TEM image for one of core-shell shaped particles with size distribution. Scale bar, 20nm. (c) SAED pattern of the particle in Figure 36(b). (d) High magnitude TEM image for CEMN. Scale bar, 5nm. (e) Number of carbon shells and nickel-to-carbon mass fraction for CEMNs. (f) High magnitude TEM images of debris. Scale bars, 10 nm and 5 nm (inset). (g) XRD profile of spark generated particles. (h) Raman spectra of spark generated particles.

Figure 37. Procedures of conventional and aerosol activation.

Figure 38. Overview of site-selective aerosol activation.

Figure 39. Schematic of copper ELD onto the line and square palladium patterns.

Figure 40. Particle size distribution of spark generated aerosol nanoparticles and collection efficiency of ACF.

Figure 41. HRTEM micrograph of spark generated nanoparticles.

Figure 42. XPS profile of spark generated aerosol nanoparticles.

Figure 43. SEM micrographs of conventionally and aerosol activated ACF.

Figure 44. EDX profiles of conventionally and aerosol activated ACF.

Figure 45. SEM micrographs of particle deposited ACF vs activation intensity.

Figure 46. SEM micrographs of particle deposited ACF vs ELD time.

Figure 47. EDX profiles of particle deposited ACF (10 min of ELD, 1.42 mg-Pd/g-ACF).

Figure 48. Results of ICP-AES analyses of silver deposited ACF.

Figure 49. Results of XRD analyses of silver deposited ACF.

Figure 50. Adsorption isotherms of silver deposited ACF.

Figure 51. Particle characterization of catalytic aerosol activation. (a) Particle size distribution of spark generated aerosol nanoparticles. (b) HRTEM image and a SAED pattern (inset) of

spark generated particles. (c) XPS profile of spark generated particles. (d) FESEM images of line and square patterns in PI substrate.

Figure 52. (a) Temperature distribution inside the area A of Figure . (b) Thermophoretic velocity distribution as a function of particle size. U is the average upstream velocity of the particle-laden flow.

Figure 53. Results of copper ELD. (a) Optical microscopy images of the copper patterns (left: slanting lines, right: square arrays). (b) FESEM micrographs corresponding to the optical microscopy images with a high-magnitude FESEM image and an EDX profile. (c) XRD profile. (d) 2D AFM profile.

Figure 54. Other copper micropatterns using different pattern masks. (a) Optical microscopy image for an angled-line array (32 μm in width). (b) Optical microscopy image for a fine circled-line (8 μm in width).

Figure 55. Overview of surface activation and particle characterization. (a) Surface activation by spark generated nanoparticles. Platinum aerosol nanoparticles were generated by a spark generator while a resistively heated YONSEI pattern mask was placed on a PI substrate cooled by a Peltier cooler. The particles were delivered to the surface of the PI substrate through the YONSEI pattern hole. (b) A temperature distribution inside the area A. (c) A particle size distribution with a HRTEM image (inset) of spark generated platinum particles. (d) A SAED pattern of the particles. (e) A XPS profile of the particles. (f) A FESEM image of YONSEI in the PI substrate.

Figure 56. Results of silver ELD. (a) A scheme of silver ELD onto the YONSEI platinum pattern. (b) A YONSEI silver pattern. (c) Optical microscopy images of YONSEI silver pattern. (d) A FESEM micrograph corresponding to the optical microscopy images. (e) An EDX profile. (f) A XRD profile.

Figure 57. Topographs of YONSEI silver pattern. (a) A 2D image. (b) A 3D image.

Figure 1S. Experimental set-up for VOC adsorption-desorption.

Figure 2S. Particle detachment characteristics during air flow (@ 0.5m/s of air velocity).

Figure 3S. VOC adsorption and desorption amounts of the pristine and the copper deposited ACF.

Figure 4S. Effective diffusivities of VOC adsorption and desorption of the pristine and the copper deposited ACF.

Figure 5S. SEM micrographs of the pristine, catalytically activated and the copper deposited ACF.

Figure 6S. EDX profiles of the pristine, catalytically activated and the copper-deposited ACF.

Figure 7S. Adsorption isotherms of N₂ at 77.4K of the pristine and the copper deposited ACF.

Figure 8S. Pore size distributions of the pristine and the copper deposited ACF.

Figure 9S. TEM micrographs of the silver deposited thin-MWNTs for (a) 3, (b) 5, and (c) 10 minutes. (d) TEM image near the open end of thin-MWNTs (for 5 minutes of ELD).

Figure 10S. Characterization of copper coated MWNTs. (a) Morphological and chemical analyses. (b) XRD profiles. (c) Adsorption isotherms and textural properties.

Figure 11S. Size distributions of spark generated particles.

Figure 12S. Spark generated particles (anode: Co, cathode: C) and their characterizations. (a) TEM image and local EDX information (inset) of the spark generated particles. (b) TEM image of the CEMN and their size distribution (inset). (c) High magnitude TEM image of the CEMN. (d) Number of graphitic shells and the Co-to-C mass fraction vs CEMN (or Co core) diameter. (e) XRD pattern and Raman (inset) spectrum of the spark generated particles.

Figure 13S. Spark generated particles (anode: Fe, cathode: C) and their characterization. (a) TEM image and local EDX information (inset) of the spark generated particles. (b) TEM image of CEMN and the size distribution (inset) of CEMN. (c) High magnitude TEM image of the CEMN. (d) Number of graphitic shells and the Fe-to-C mass fraction vs CEMN (or Fe core) diameter. (e) XRD and Raman (inset) spectra of the spark generated particles. (f) TEM images of the spark-generated multiwall carbon nanotubes.

Figure 14S. Thermophoretic velocity distribution as a function of particle size. U is the average upstream velocity of the particle-laden flow.

Figure 15S. Other silver patterns using different pattern masks. (a) An optical microscopy image for silver square arrays ($65 \times 65 \mu\text{m}^2$). (b) An optical microscopy image for a ultrafine silver line ($4 \mu\text{m}$ in width).

List of Tables

Table 1 Textural properties of the pristine and copper-deposited ACF

Table 2 Amounts and crystal sizes of the silver particles deposited onto thee ACF discs

Table 3 Adsorptive properties of the silver deposited ACF discs

Table 4 Diameters of the inhibition zones of the silver deposited ACF discs (Mean \pm SD)

Table 5 Textural properties of the silver coated MWNTs

Table 6 Generation rates of monometallic nanoparticles with relating parameters

Table 7 Metal fractions and generation rates of bimetallic nanoparticles

Table 8 Properties of the graphite rod, the generated carbon particles, and conventional activated carbon

Table 9 Data η and R based on pore volume

Table 10 Crystal sizes (nm) of silver particles vs activation intensity and ELD time

Table 11 Textural properties of silver deposited ACF vs activation intensity and ELD time

Table 1S Textural properties of copper-deposited ACF

Table 2S Table 2S Yields of CEMN as a function of the metal-to-carbon mass fraction

Abstract

Activated carbon fibers (ACF) were activated with Pd-Sn catalytic nuclei in a single-step process. The catalytically activated ACF were then used as supporters in the specific, electroless deposition (ELD) of fine copper or silver particles. The amount of metal particles was easily controlled by regulating the deposition time. For NO removal, pitch-based ACF were used as supporters for copper nanoparticle deposition. For antibacterial action and volatile organic compounds (VOC) adsorption-desorption, rayon-based ACF were used as supporters for copper or silver nanoparticle deposition. Furthermore, a progress of metallization on multiwall carbon nanotubes (MWNTs) during electroless deposition was investigated when the deposition time increased from 3 to 10 minutes. Results show that the metallization of face-centered cubic silver (or copper) on MWNTs progressed from interior surfaces to exterior surfaces of the MWNTs.

Spark generation (SG) was used to synthesize various aerosol nanoparticles. First, generation and characterization of monometallic (palladium, platinum, gold, and silver from homogeneous spark sets) and bimetallic (palladium-platinum, palladium-gold, and palladium-silver from heterogeneous spark sets) nanoparticles dispersed in nitrogen gas by spark generation method were reported. Next, an idea of gas-to-particle removing benzene, toluene and xylene (BTX) gas in a controllable way through carbon aerosol particles produced by a spark generator was introduced. Finally, an aerosol synthesis method of carbon-encapsulated metal nanoparticles (CEMNs) via metal-graphite sparks in a continuous manner without the use of vacuum with special operating conditions was presented. The method was both simple and continuous, and constituted a more practical method to prepare CEMNs than conventional ones, and therefore, can be applied in order to produce nanocrystal encapsulates.

A method of catalytic activation with palladium aerosol nanoparticles produced by spark generation was introduced. These catalytic particles were deposited onto the surfaces of ACF. After thermal curing, the catalytically activated ACF were placed into a solution for ELD of silver. Homogeneous silver coatings on ACF were achieved under various activation intensities and ELD times, and the results were compared to those obtained with a conventional “two-step” activation. Furthermore, a simple and environmentally benign method of site-selective catalytic activation by producing palladium (or platinum) aerosol nanoparticles via spark generation and then thermophoretically depositing the particles onto a flexible polyimide (FPI) substrate through the pattern holes of a mask was introduced. After annealing, the activated substrate was placed into a solution for electroless copper (or silver) deposition.

Key Words: Nanoparticle synthesis; Electroless deposition; Spark generation

1. Nanoparticle synthesis by electroless deposition (ELD)

1.1 Introduction

1.1.1 ELD of copper (Cu) onto pitch-based activated carbon fibers (ACF)

Porous carbon materials, due to their extensive specific surface area, high adsorption capacity, microstructure, and special surface reactivity, have been widely used in separation, purification, and catalytic processes [Park & Kim, 2005a]. Activated carbon fibers (ACF), highly microporous carbon materials [Chen & Zeng, 2003; Moon et al., 2000; Yang & Kaneko, 2002], are commercially available in the form of fiber tows, cloths (fabrics), papers, mats and felts [Matatov-Meytal & Sheintuch, 2002]. ACF have a larger micropore volume and a more uniform micropore size distribution than granular activated carbons (GAC) and; thus, are considered to have a larger adsorption capacity and greater adsorption and desorption rates [Fu et al., 2004; Li et al., 1998; Mochida et al., 2000; Park et al., 2004; Shen et al., 2006; Vilaplana-Ortego et al., 2002].

The ACF may be packed or constructed to fit almost any geometry for almost any catalytic application and satisfies the requirements of high catalyst effectiveness and a low pressure drop for finely divided catalysts, but avoids the technical problems associated with powders. For example, the ACF may be employed for the removal of NO_x [Guo et al., 2001; Lee et al., 2002; Mochida et al., 2001; Shirahama et al., 2002 & 2004], but only physically adsorbs a limited amount of NO because of the weak interactions between the two [Adapa et al., 2006; Zawadzki & Wiśniewski, 2002]. In order to effectively remove NO, enhancing the

NO reduction activity of ACF is an important factor. The reduction of NO by ACF is closely related to its surface chemical properties. The catalytic reduction of NO to N₂ and O₂ using ACF employing a transition metal (Ni, Fe, Cu, or Pd) prepared by the impregnation and precipitation of an aqueous solution of the metal, has previously been investigated [Park & Kim, 2005a], copper has been shown to possess the most efficient catalytic activity toward the reduction of NO to N₂ and O₂, both with and without O₂ [Illán-Gómez et al., 1996; Marquez-Alvarez et al., 1996].

Recently, electrolytic metal deposition, of an aqueous solution of metal ions, has been proposed as a useful method for the introduction of a metal onto carbon surfaces and into carbon micropores [Park & Kim, 2005a & 2005b]. Electroless metal deposition, a form of electrolytic metal deposition, can be effective for coating the ACF [Lin et al., 1997; Norkus et al., 2006; Park & Kim, 2005b]. Electroless metal deposition refers to the deposition of a metal onto a substrate, without an external electric current, via oxidation-reduction reactions [Zhao et al., 2006]. This procedure can yield mechanically durable catalyst layers with high specific surface areas, which may be catalytically activated. The electroless deposition technique enables catalytic components to be easily and uniformly deposited in some channels of supporter with a complex configuration, provided that the deposition solution is in contact with the channel walls [Fukuhara et al., 2005].

For the stable deposition of fine metal particles onto the ACF, the catalytic activation method proposed by Ang et al. (1999) and Xu et al. (2004) was employed. These two investigations studied the coating of carbon nanotubes with nickel and copper, and copper, respectively. The nanotubes were activated in one activation bath (single-step process). The conventional activation process consisted of a two-step process, Sn-sensitization and Pd-activation, and uses two separate colloidal solutions. In this section, a single-step process was

used to catalytically activate the ACF and; thus, to introduce active sites onto the ACF surfaces for the electroless copper deposition [Byeon et al., 2007a]. After the ACF surfaces had been sensitized with Sn^{2+} ions (Sn^{2+} sensitization), these were oxidized to Sn^{4+} , with the simultaneous reduction of Pd^{2+} ions to metallic Pd (Pd activation), which adhered to the ACF surface in the form of fine Pd particles. After the Pd activation step, Cu^{2+} ions were introduced, and then reduced into metallic Cu on the Pd particles that had been predeposited onto the ACF. The metallic Pd sites worked effectively in the electroless deposition of copper due to the galvanic displacement of the metallic Pd by Cu [Zhao et al., 2006; Charbonnier et al., 2006].

In this section, pitch-based ACF were first coated with fine particles using electroless copper deposition and then characterized by field emission scanning electron microscopy (FESEM), energy dispersive X-ray spectroscopy (EDX), X-ray diffractometry (XRD), nitrogen adsorption and inductively coupled plasma atomic emission spectroscopy (ICP-AES) analysis.

1.1.2 ELDs of Cu and silver (Ag) onto rayon-based ACF

Microorganisms collected on filter surfaces could affect the integrity of the filters and the release of microorganisms [Verdenelli et al., 2003], so antibacterial treatment has to be applied to the air filter media in order to improve the air quality. Park and Jang (2003), Tamai et al. (2001) and Li et al. (1998) have reported that bacteria preferably adhere to the solid carbon material. Moreover, Cecchini et al. (2004) and Verdenelli et al. (2003) reported that bacteria can adhere to glass acrylic fiber. Previous studies [Stoimenov et al., 2002; Zhang et al., 2004] have shown that antibacterial formulations only in the form of fine particles could be used as effective antibacterial materials. In this section, ACF made of a type of highly microporous carbon material [Norkus et al., 2006] were chosen, as the air filter medium. Fine copper particles were selected as the antibacterial material [Park & Kim, 2005a]. The particles

were forced to deposit on the ACF to prevent bacteria from breeding on the surface of the ACF. Previous studies [Ang et al., 1999] have focused on the preparation and characterization of antibacterial materials rather than the method of deposition of antibacterial materials on the ACF.

Bioaerosols are airborne particles of biological origins, including viruses, bacteria, fungi and all varieties of living materials. In suitable hosts, bioaerosols are capable of causing acute or chronic diseases, which may be infectious, allergenic or toxigenic [Main, 2003]. Numerous engineering solutions are commercially available for the removal of bioaerosols, and others are under development such as air filtration, ultraviolet germicidal irradiation (UVGI), negative air ionization, electrostatic precipitation, photocatalytic oxidation and air ozonation, etc [Griffiths et al., 2005; Walker & Ko, 2007].

Indoor air bioaerosols accumulate in large quantities on filters of heating, ventilating and air-conditioning (HVAC) systems where they are able to multiply under certain conditions; especially if high amounts of moisture are present on the filter [Maus et al., 2001]. Moreover, the organic or inorganic materials deposited on the filter medium after air filtration contribute to microbial growth. This inevitably leads to decreased filter efficacy and, probably, to deterioration of the filters, with the eventual release of microorganisms. Volatile organic compounds (VOC) produced by microbial metabolism (MVOC) can be emitted from the contaminated filters [Verdenelli et al., 2003].

As an effective antimicrobial agent, silver is believed to interact with elements of the bacterial membrane, causing a structural change, dissipation of the proton motive force and finally to cell death [Sondi & Salopek-Sondi, 2004; Lok et al., 2006]. Because of the antimicrobial activity of silver, many silver-containing materials have been developed for antimicrobial applications [Jeon et al., 2003; Zhang et al., 2004; Morrison et al., 2006; Wang

et al., 2006]. In this section, rayon-based ACF containing copper or silver particles were prepared using an ELD and their efficacy for antimicrobial action was tested. Finally, the adsorption and desorption characteristics for removing VOC via the prepared copper deposited ACF were studied.

1.1.3 ELDs of Cu and Ag onto multiwall carbon nanotubes (MWNT)

Since MWNTs are an ideal raw material for various applications owing to their outstanding properties [Wang et al., 2004], the functionalization of MWNTs with metal nanoparticles has attracted ever-increasing interest [Guo & Li, 2005; Ma et al., 2006; Terrones, 2004; Wildgoose et al., 2006]. Metal particle-supported MWNTs are expected to be potential future materials [Qu and Dai, 2005; Ye et al., 2003] for hydrogenation catalysis or as materials in fuel cells, Li-ion batteries, supercapacitors, magnetic recording, reinforcements or for microwave absorption [Guo & Li, 2005; Planeix et al., 1994; Wildgoose et al., 2006; Xu et al., 2004]. Various metal nanoparticles have been reported recently, such as Cu [Ang et al., 1999 & 2000; Xu et al., 2004], Ni [Ang et al., 2000], Pt [Matsumoto et al., 2004; Porter et al., 2002], and Au [Jiang & Gao, 2003; Ma et al., 2006; Porter et al., 2002]. Previous approaches to functionalizing MWNTs with metal nanoparticles [Choi et al., 2002; Day et al., 2002; Fullam et al., 2000; Pradhan et al., 1998; Xu et al., 2003] include physical evaporation, attachment after the oxidation of nanotubes, a solid state reaction with metal salts at elevated temperatures, and ELD from salt solutions using reducing agents or catalyst [Choi et al., 2002; Hasegawa et al., 2007; Kim & Sigmund, 2004].

ELD is of particular interest because its simplicity can facilitate the large-scale production of nanotube-nanoparticle hybrids [Ebbessen et al., 1996; Qu and Dai, 2005; Wildgoose et al., 2006]. The ELD technique is particularly appealing because of its low cost, inherent selectivity and ability to deposit high quality films on very thin seed layers [Xu et al., 2002]. Thus far experimental studies have focused mainly on final or fully- metal deposited MWNT and their specialized applications. However, there are few reports showing the progress of metallization of MWNTs. The detailed structure and location of metal nanoparticles along a nanotube plays an important role in determining the final assembled structure and its performance [Qu et al., 2006]. Studies on the progress of metallization during the ELD process are needed in order to gain better understanding of the metallization of MWNTs.

In this section, silver deposited MWNTs were prepared using a nitric acid-treatment, Sn-Pd activation, hydrochloric acid-acceleration, and ELD of silver. Details of the aforementioned processes are reported in [Supplementary Data 2](#). High resolution transmission electron microscopy (HRTEM), EDX and X-ray diffraction XRD were used to characterize the morphology and structure of the silver coated MWNTs. The textural properties of the MWNTs during the ELD process were examined using the Brunauer, Emmett, and Teller (BET) method.

1.2 Materials and methods

1.2.1 Preparations and characterizations of Cu deposited ACF and a test for NO removal

Pitch-based ACF were synthesized using a conventional melt-blown spinning method. The fibers, 1mm in diameter, were produced, using extruding melt (IPP; SK Chemical Co., Korea) through a round-shaped mono-hole spinneret ($L/D = 2$, $D = 70$ mm), under pressurized nitrogen at 6 kg/cm^2 , 673 K, with subsequent drawing at a take-up speed of 550 m/min. The melt-blown spinning pitch fibers were then oxidatively stabilized in air by heating to 673 K at 1 K/min for 2 hours. The stabilized pitch fibers were then carbonized by heating in an N_2 atmosphere to 1,273 K at 10 K/min for 30 minutes. After holding the carbonized fibers at 1,223 K for 30 minutes, they were finally activated in steam (50 vol.%) carried by N_2 . These ACF were washed with deionized water and dried overnight at ambient temperature.

Since the bond strength of the copper particles on the ACF was very sensitive to surface contamination, the ACF were thoroughly degreased by immersing in a diluted degreasing agent bath (50 mL of CC829, Yooil Material Technology, Korea, mixed with 950 mL of DI water) at 327 K for 10 minutes. After washing the degreased ACF three times with DI water, the palladium and tin species were introduced onto by immersing in a mixed Pd-Sn colloidal solution at 318 K for 6 minutes. A solution (30 mL of CATA1064, Yooil Material Technology, Korea) diluted with 1 M of nitric acid (970 mL) was used as a mixed Pd-Sn colloidal solution. The catalytically activated ACF were immersed in an acceleration solution bath (50 mL ACCEL95, Yooil Material Technology, Korea, diluted to 1,000 mL with DI water) for 7 minutes at 298 K and then washed with DI water a further three times. The acidic accelerator was used to preferentially dissolve the protective layer (mainly Sn layer), exposing

a greater surface area of the catalytic Pd nuclei. When the catalytically activated, accelerated ACF were immersed in an electroless deposition bath, copper was deposited at the catalytic sites, with copper particles-deposited ACF finally obtained. The deposition bath (1 L) consisted of copper sulfate dominant solution (120 mL EC1051A, Yooil Material Technology, Korea, diluted to 500 mL with DI water) and formaldehyde dominant solution (110 mL EC1051B, Yooil Material Technology, Korea, diluted to 500 mL with DI water) at 298 K for various treatment times ranging from 0 to 20 minutes.

To study the surface structures of the ACF, wide-angle XRD patterns of the ACF were obtained with a Rigaku Model D/MAX-Rint 2000 (Japan) diffraction meter using $\text{CuK}\alpha$ radiation ($\lambda = 0.15418 \text{ nm}$) at 30 kV and 20 mA. A thin powder sample of the ACF was placed onto an oriented monocrystalline quartz plate and scanned from 10° to 80° (2θ) at $4^\circ/\text{min}$. A FESEM (JSM-6500F, JEOL, Japan) was used to observe the surface morphology of the ACF as well as the distribution of copper particles. A chemical analysis was performed using EDX (JED-2300, JEOL, Japan). The amount of copper particles on the ACF sample was determined using an ICP-AES (Elan 6000, Perkin-Elmer, US). About 0.1 g of the sample was dissolved in 50 mL nitric acid, and the diluted to 100 mL with DI water. After three hours, the sample was filtered, with the remaining mixture delivered for ICP-AES analysis. The nitrogen adsorption isotherms of an ACF sample were measured using a porosimeter (ASAP 2010, Micromeritics Ins. Corp., US) at 77.4 K with relative pressures ranging from 10^{-6} to 1. High purity (99.9999%) nitrogen was used for a material to be adsorbed. All samples were degassed at 573 K for two hours before each measurement. The specific surface area was determined using the BET equation. The total pore volume, which was estimated on the basis of the N_2 volume adsorbed at a relative saturation pressure (~ 0.996), actually corresponded to the total amount adsorbed. The pore size distribution was determined using the Barrett, Joyner, and Halenda

(BJH) method, which uses the area of the pore walls and the Kelvin equation to correlate the relative N_2 pressure at equilibrium with the amount of porous solid, with the size of the pores of capillary condensation takes place.

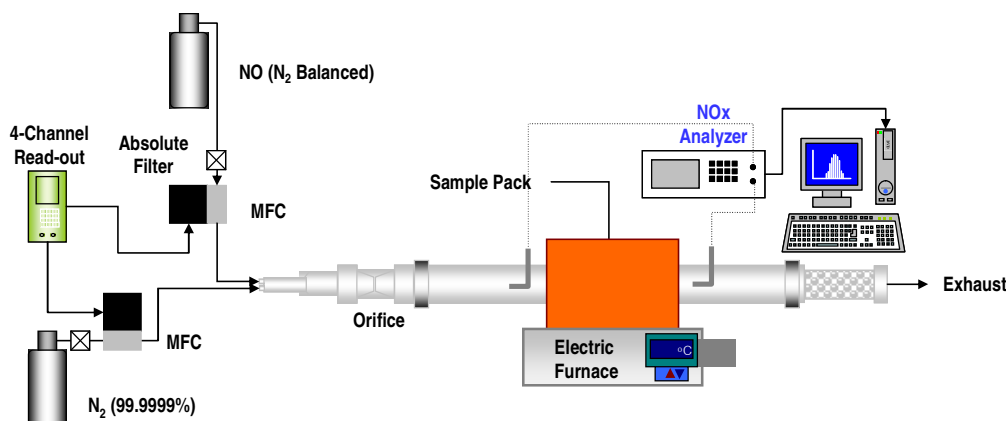


Figure 1. Diagram of the experimental setup for the NO removal test.

Figure 1 shows the experimental setup used for the NO removal test. For each experiment, 3 g of the prepared ACF (140 mm in length) was initially inserted into a quartz tube reactor (10mm in diameter and 500 mm in length) and heated under a N_2 flow at 423 K for one hour inside an electric furnace (1 kW). The wall temperature of the reactor was varied from 423 to 673 K using a proportional integral derivative (PID) temperature controller. Stainless steel (SS) mesh was used to support the ACF and minimize the channeling phenomenon. Model NO gas in N_2 at room temperature was delivered to the reactor and mixed with N_2 (99.9999%) gas, resulting in a NO concentration of 160 ppm at the reactor inlet. Absolute filters were used to filter out contaminant particulate matters existing in the test gases. The total gas flow rate through the reactor was maintained at 3 L/min by adjusting two mass

flow controllers (MKS Instrument, US). An orifice was used to promote mixing of NO and N₂ fluid dynamically.

The concentration of NO was continuously measured using a chemiluminescence NO analyzer (Thermo Electron Instruments Inc., Model 42c, US), which monitors NO, NO₂ and NO_x at a sampling rate of 0.7 L/min. The NO removal efficiency was determined by measuring the concentration of NO at the outlet of the reactor. Experiments were repeated four times, with the average values reported.

1.2.2 Preparations and characterizations of Cu and Ag deposited ACF and tests for antibacterial action and VOC adsorption-desorption

The rayon-based ACF studied in this work were manufactured by Toyobo (KF-1500, Japan). ELDs of metals onto the ACF were performed in a laboratory by using commercial electroless copper [Byeon et al., 2007b] and silver [Byeon et al., 2007c] solutions. Details of the copper deposition procedure are presented in [Supplementary Data 1](#).

- Copper deposited ACF

The antibacterial activity trend of these prepared ACF samples was determined by using the modified Kirby-Bauer agar diffusion method [Verdenelli et al., 2003]. Four experimental bacterial strains were used, i.e., two Gram-negative strains (*E.coli*, ATCC 11775 and *P.fluorescens*, ATCC 13525) and two Gram-positive strains (*B.subtilis*, ATCC 6633 and *M.luteus*, ATCC 10240). Samples of the pristine and copper deposited ACF were cut into discs (diameter: 10 mm) and sterilized with UV light. A constant volume (100µ L) of culturing

solution containing the bacteria concentration of 10^8 cells/mL was injected on a 50mm diameter nutrient agar plate (composition in gL⁻¹; beef extract 3, peptone 5 and agar 15 at pH 6-8 (DIFCO Laboratories, US)). Each copper-deposited ACF disc was placed on the lawn of bacteria of the agar plate and incubated for 72 hours at 303 K. The antibacterial activity was first examined by observing the growth of bacterial colonization near the prepared ACF sample. The diameter of the inhibition zone of the bacterial colonization was then measured. The experiments were repeated four times and the same procedure was applied to the other bacterial strains. The concentrations of VOC gases [Byeon et al., 2006] were continuously measured (see the [Supplementary Data 1](#)) by a photoionization detection (PID) gas analyzer (Kinsco Inc., Sniffer II, Korea), which monitored the TVOC at a sampling flow rate of 0.5 L/min. The TVOC gas analyzer has a performance range of 0-10 ppmv and a lower detection limit (LDL) of 0.01 ppmv. The PID output was measured and recorded at 1 Hz by using a data logger.

- Silver deposited ACF

Silver was coated on the ACF discs (KF-1500, Toyobo, Japan) using an electroless deposition method. The samples denoted as Ag-10, Ag-20 and Ag-30 were prepared without the use of electric current at deposition times of 10, 20 and 30 minutes, respectively, with silver metal solution. Before the electroless silver deposition, the ACF discs were catalytically activated by immersion for 5 minutes at 25°C in an aqueous solution containing palladium to maximize the autocatalysis [Park et al., 1999].

Escherichia coli (ATCC 11775) and *Bacillus subtilis* (ATCC 6633) were selected as model Gram-negative and Gram-positive bacteria, respectively. For each bacterium, a bacterial suspension was prepared by culturing 0.1 mL of an overnight culture, inoculated in 15 mL of

nutrient broth, for 18 hours. The nutrient broth was prepared by dissolving 5 g of peptone and 3 g of meat extract in 1000 mL of sterilized deionized water and then by sterilizing the solution with an autoclave.

Figure 2 shows a schematic diagram of experimental setup for the pressure drop and filtration tests. For bioaerosol generation, the prepared bacterial suspensions were washed three times with sterilized deionized water using a centrifuge (VS-1500N, Vision Scientific, Korea) at 6,000 rpm for 15 minutes, to remove the residual particles including the components of the nutrient broth. The washed suspensions were then diluted with sterilized deionized water, to give suspensions with an optical density of 0.01 at 600 nm as measured using a spectrophotometer (SP-300, Optima, Japan). A bacterial mixture of *E. coli* and *B. subtilis* (1:1 ratio) was nebulized using a Collison-type nebulizer (1 jet, BGI Inc., US) at a flow rate of 2 L/min and introduced into a dilutor. Dispersed bioaerosols were diluted and introduced into the test duct where a prepared ACF disc was installed. The face velocity was controlled from 0.1 to 0.5 m/s using a mass flow controller. The air used in this study was dried and cleaned using a clean air supply system that consisting of oil trap, diffusion dryer and HEPA (High Efficiency Particulate Air) filter.

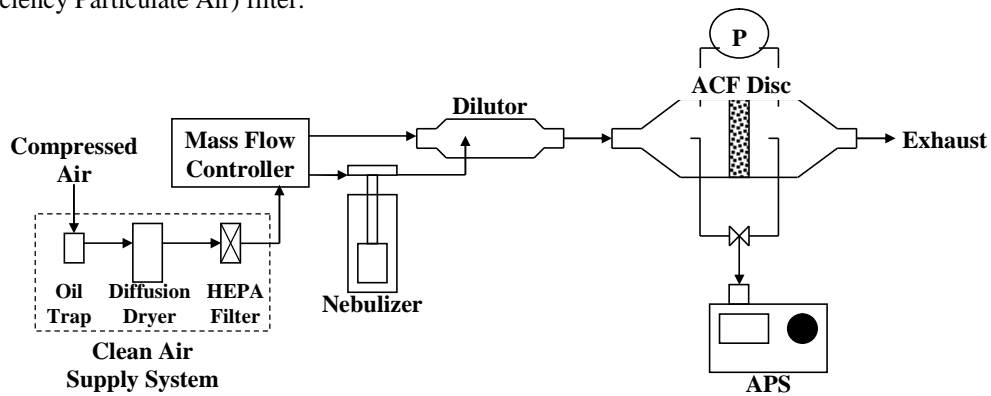


Figure 2. Experimental set-up for tests of pressure drop and filtration.

The pressure drop across the filter was measured using a differential pressure gauge. The number concentrations of the bioaerosols were measured at upstream and downstream of the filter using an aerodynamic particle sizer (APS; model 3321, TSI Inc., US). The overall particle filtration efficiency (η) is defined as follows;

$$\eta = 1 - C_{\text{down}}/C_{\text{up}} \quad (1)$$

where C_{down} and C_{up} are the number concentrations of the bioaerosols measured at downstream and upstream of the filter, respectively.

Antimicrobial tests on the silver-deposited ACF discs were performed using the disc-diffusion method [Melaiye et al., 2005]. Nutrient agar, made by dissolving 5 g of peptone, 3 g of meat extract, and 15 g of bacto agar in 1000 mL of deionized water, was used to culture the bacteria after autoclave. 0.1 mL of the prepared bacterial suspension for *E. coli* or *B. subtilis* was spread on the nutrient agar plate. The test filter was placed on the lawn of bacteria and incubated overnight. The antimicrobial activity was observed by visually inspecting the diameter of the inhibition zone around the filter.

The time-dependent antimicrobial characteristics were investigated using the colony counting method. 10^6 cells were inoculated onto the test filter and incubated for the contact times of 0, 2, 5, 10, 60, 120, and 240 minutes, at room temperature and 70% relative humidity. After the contact time had elapsed, the test filter was immersed in 50 mL of sterilized deionized water in a sterilized plastic bag (BagLight, Interscience, France), with the bag then stroked by a BagMixer (400VW, Interscience, France) for 3 minutes, at a speed of 9 strokes/sec. The bacteria separated from the test filter were then spread on a nutrient agar plate, incubated for 24 hours and a colony analysis performed.

1.2.3 Preparations and characterizations of Cu and Ag deposited MWNT

The MWNTs were synthesized by a Korean company (Nanokarbon Co., Ltd.) using a catalyst assisted chemical vapor deposition (CVD) procedure followed by heat-treatment at 2800°C under an argon flow for 30 minutes to form the graphite layer structure. The mean diameter and length of the MWNTs was ~75 nm and 20 µm, respectively. Due to the strongly hydrophobic nature of MWNTs, an appropriate treatment of the MWNTs for activating their surfaces prior to the ELD process is essential for bonding metal particles to them. Figure 3(a) shows the experimental procedure for silver ELD onto the MWNTs.

The cleaning and surface modification of the as-purchased MWNTs were carried out using diluted nitric acid (16 M) to produce adequate interface strength between the nanotubes and metals. The acid treatment was reported to produce –COOH, –OH, –C=O and other oxygen-containing functional groups [Chen et al., 2006] on the surfaces of the MWNTs [Chen et al., 2006; Feng & Yuan, 2004; Guo & Li, 2005; Pradhan et al., 1998; Xing, 2004; Xu et al., 2006; Yu et al., 1998]. Sn-Pd activation (so-called “one-step” process) of the acid-treated MWNTs was carried out as proposed by Ang et al. (1999 & 2000) to catalyze the surfaces of the MWNTs and promote the subsequent ELD of silver. The MWNTs were stirred in a solution containing a mixture of 60 mL Sn-Pd colloid (28 mL of 0.5 M SnCl₂, 28 mL of 0.025 M PdCl₂, and 4 mL of 1 M HCl). During Sn-Pd activation, SnCl₂ was deposited onto the surfaces of the MWNTs while PdCl₂ was reduced by SnCl₂ according to the following reaction: $\text{Pd}^{2+} + \text{Sn}^{2+} \rightarrow \text{Sn}^{4+} + \text{Pd}^0$. The resulting Pd particles serve as seeds for catalytic nucleation. After the MWNTs had been accelerated using a dilute HCl (1 M) solution, and washed using 100 mL deionized (DI) water, they were then immersed into a solution for the

ELD of silver. The Pd particles on the surfaces of the MWNTs would reduce silver ions to silver atoms, where silver is further formed homogeneously (autocatalytic process). All processes including the HNO₃-treatment, Sn-Pd activation, and HCl acceleration, and ELD were performed in a 200 mL microfiltration unit, as shown in Figure 3(b). Each process time was determined by controlling the suction rate of the vacuum pump. The process times for the HNO₃-treatment, Sn-Pd activation, and HCl-acceleration steps were 5, 6, and 3 minutes, respectively. The ELD time was varied from 3 to 10 minutes. Microfiltration was performed through a polytetrafluoroethylene (PTFE) membrane (Milipore, 0.22 μm pore size). Mechanical agitation during each process enhanced the dispersion of MWNTs in each solution. All the above processes were operated at 20°C. Finally, the silver coated MWNTs were washed three times in DI water and dried at 70°C for 24 hours.

A drop of a solvent containing the MWNTs was placed onto carbon-coated copper transmission electron microscopy (TEM) grids. The morphology of the MWNTs was analyzed by TEM (JEM-2010) operated at 200 kV and a high resolution TEM (HRTEM, JEM-3010) with an energy dispersive X-ray spectroscope (EDX, Oxford) operated at 300 kV. X-ray diffraction (XRD) of the silver (or copper) coated MWNTs were carried out using a Rigaku RINT-2100 diffractometer equipped with a thin film attachment using Cu-K α radiation (40 kV, 40 mA). The 2 θ angles ranged from 10 to 90° with a speed of 4°/min by step scanning at an interval of 0.08°. The crystallite size of the silver (or copper) particles was calculated from the XRD spectra using the Scherrer formula ($t=0.9\lambda/(B\cos\theta)$). The nitrogen adsorption isotherms of the MWNTs were measured using a porosimeter (ASAP 2010, Micromeritics Ins. Corp., US) at 77.4K at a relative pressure ranging from 10⁻⁶ to 1. High purity (99.9999%) nitrogen was used. All the samples were out-gassed at 573 K for two hours before each measurement. The specific surface area was determined using the BET equation. The total pore volume,

which was estimated based on the N_2 volume adsorbed at a relative saturation pressure (~ 0.996), corresponded to the total amount of N_2 adsorbed. The pore size distribution was determined using the BJH method, which uses the area of the pore walls, and it employs the Kelvin equation to determine the correlation between the relative N_2 pressure in equilibrium and a porous solid with a pore size suitable for capillary condensation to occur.

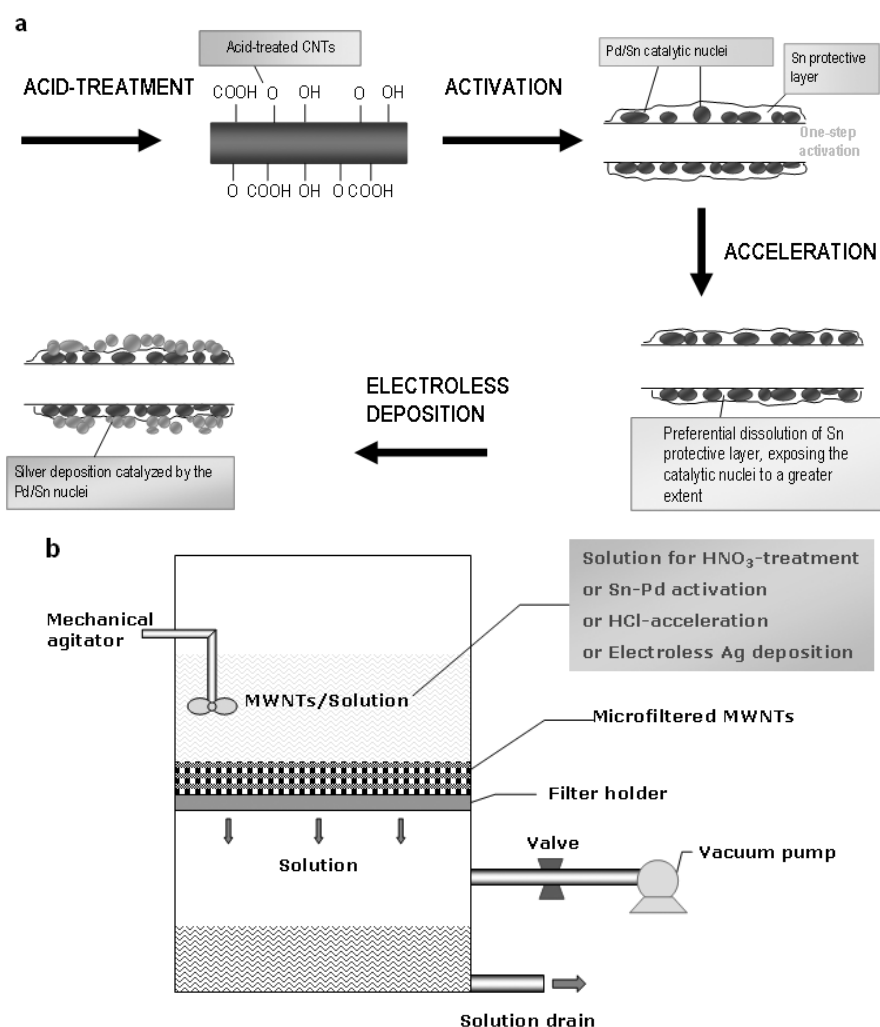
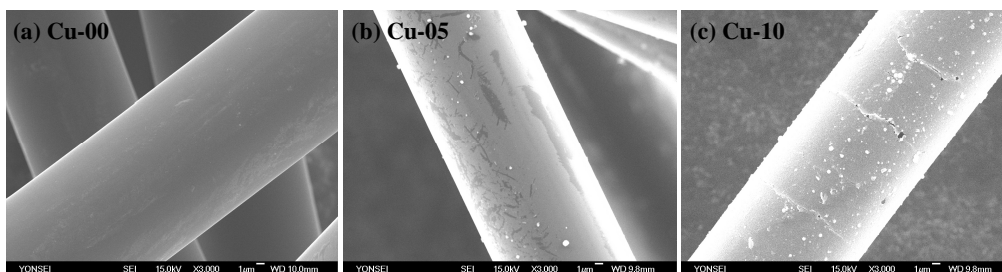


Figure 3. (a) Processes for silver metallization. (b) Schematic diagram of the microfiltration unit.

1.3 Results and discussion

1.3.1 ELD of Cu onto pitch-based ACF and an application for NO removal

Figure 4 show FESEM micrographs of the prepared ACF samples where Cu-05, Cu-10, Cu-15 and Cu-20 represent copper coated ACF for deposition times of 5, 10, 15 and 20 minutes, respectively, while Cu-00 represents pristine ACF. With increasing deposition time, more particles were deposited onto the surface of a fiber, which grew larger, with snowflake-shaped particles or aggregates of 50nm-1 μ m observed, as shown in Figures 4(c) and 4(e). The SEM micrographs revealed copper particles, as examined by EDX analyses, as shown in Figure 5. The EDX results showed that an ACF sample contained carbon, copper and a small amount of oxygen. The observed oxygen may have originated from melt-blown fibers becoming ACF prior to the electroless deposition. Figure 5 shows that with Cu-00 no copper peak was observed, but the copper-deposited ACF samples had some CuKa and CuLa, etc. peaks, indicating the presence of copper in the ACF samples. The Cu-05 and Cu-10 samples also contained a small amount of tin, which may have originated from the Pd-Sn activation. However, it was interesting that no tin was detected for deposition times longer than 10 minutes implying the Cu-15 and Cu-20 ACF samples used for the analysis were entirely covered with copper.



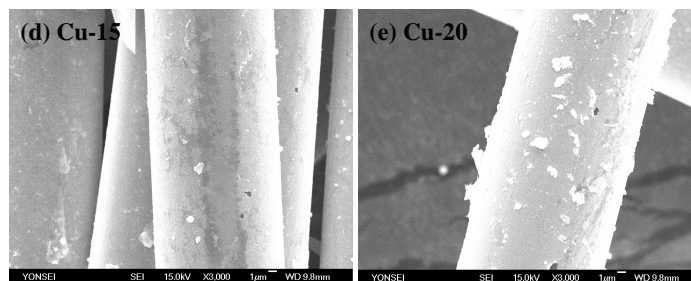


Figure 4. FESEM micrographs of the pristine and copper deposited ACF.

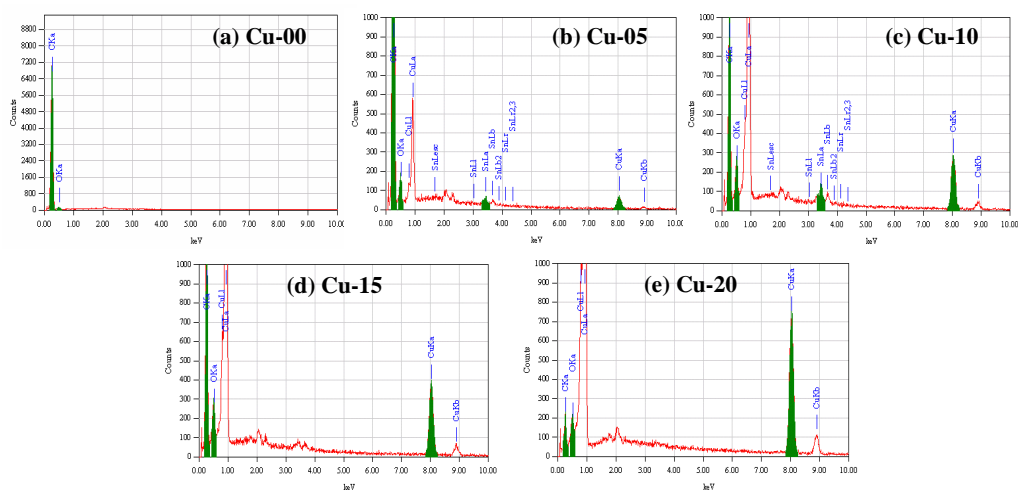


Figure 5. EDX profiles of the pristine and copper deposited ACF.

The surface structures of the copper particles deposited ACF samples were also studied using the wide-angle XRD method. Figure 6 shows sharp peaks at around $2\theta = 43^\circ$, 50° , and 74° , which corresponded to the [111], [200], and [220] planes of the copper (JCPDS 4-836) on the ACF surfaces, respectively. The average crystallite sizes estimated from the XRD line broadening of the [111] peak, according to Scherrer's equation, were 3.97, 6.85, 12.44, and

14.95 nm for copper deposition times of 5, 10, 15, and 20 minutes, respectively. The sharpness of the copper peaks proved that the copper particles had a nearly perfect crystal structure. The intensities of the copper peaks increased with deposition time, which was caused by the growth of the copper particles. The intensity of the copper peaks and the crystallinity of the copper deposited ACF were strengthened with increasing deposition time. From the ICP-AES analyses, the mass of copper per unit mass of ACF was obtained. Figure 7 shows that the amount of copper increased with increasing deposition time.

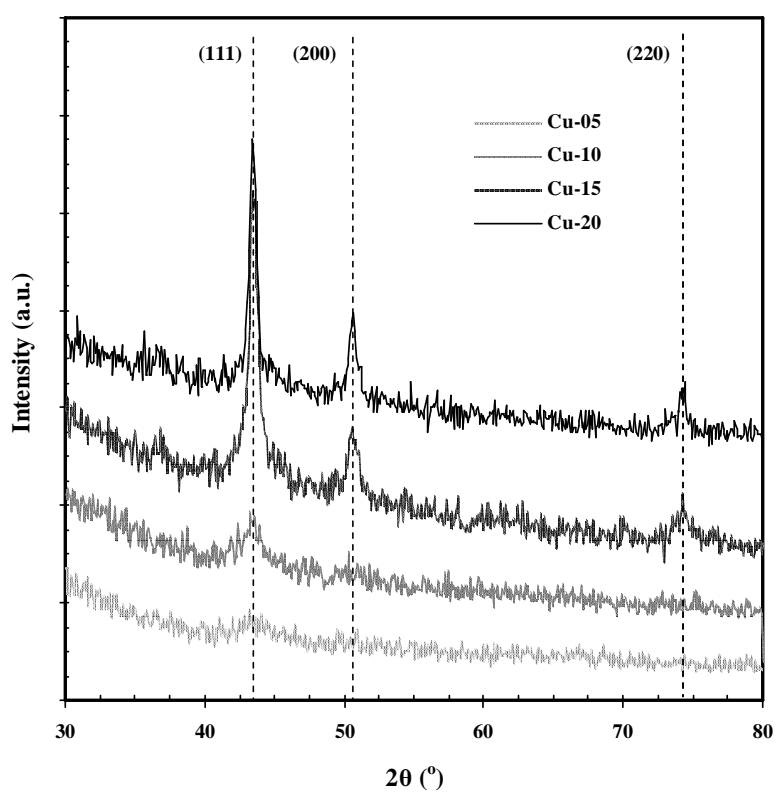


Figure 6. X-ray diffraction patterns of the copper deposited ACF.

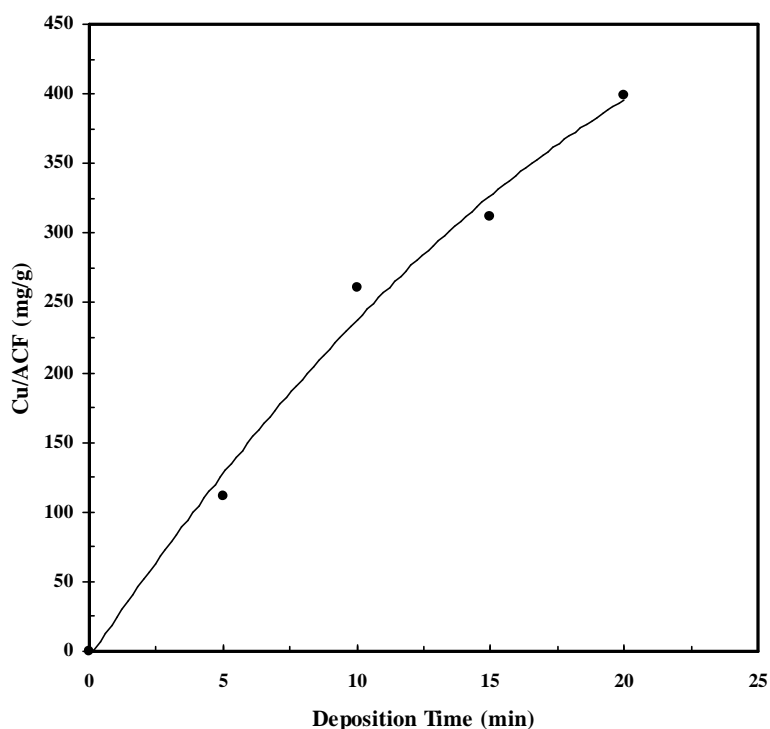


Figure 7. Amount of copper as a function of the deposition time (by ICP-AES analysis).

Once the copper deposited ACF had been characterized, they were applied as catalyst fibers to enhance the NO removal efficiency. Figure 8 shows the results under various temperature conditions. The test NO gas was injected into the reactor at a concentration of 160 ppm (N_2 balance). When no copper particles existed on the ACF, NO was adsorbed onto the surface of the carbon fibers, and this adsorption slightly increased with increasing temperature. However, after about 4 minutes, the adsorption drastically decreased at all temperatures. When copper particles existed on the ACF, in addition to the adsorption by the carbon fibers, NO, which was adsorbed onto the carbon fibers, would transfer to the neighboring copper particles

by surface diffusion, resulting in the catalytic reduction of NO around the copper particles. For temperatures below 473 K, the amount of copper on the ACF had little effect on the removal of NO. However, when the temperature was equal to or higher than 573 K, more NO was removed with the copper-deposited samples. At a reaction temperature of 673 K, the removal efficiencies at the steady state were 80-90%. Of note: for temperatures between 573 and 673 K; however, the highest removal efficiency was achieved with the Cu-05 sample, even though the amount of copper, acting as a catalyst, was lowest. The removal efficiency decreased as the amount of copper was further increased.

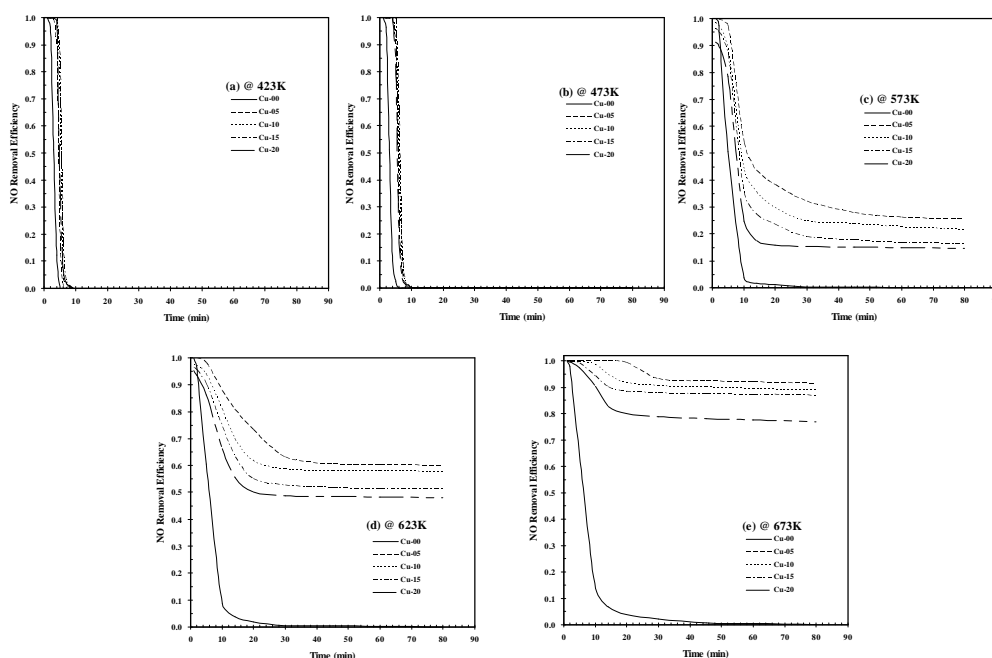


Figure 8. NO removal characteristics of the pristine and copper deposited ACF.

To understand the adverse effect of an excessive amount of copper on the removal of NO, the porosity and specific surface area properties of the copper deposited ACF were

measured. Figure 9 shows that the greatest uptake occurred at a relatively low pressure ($P/P_0 < 0.1$) and reached a plateau at $P/P_0 \approx 0.3$, implying that all the ACF samples, according to the IUPAC classification, had microporous characteristics (type I isotherm) [Brunauer et al., 1938]. The specific surface area was largest for the Cu-00, and decreased with increasing amount of copper as the deposited copper particles could block or take up some pores of the corresponding ACF support.

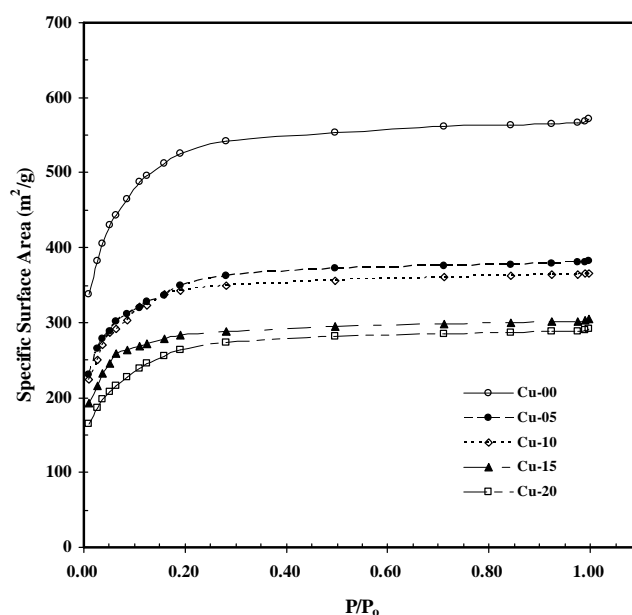


Figure 9. Pore size distributions of the pristine and copper deposited ACF.

The pore size distributions of the samples were also measured. Figure 10 shows that the pore size distributions of all the samples were concentrated at pore diameters smaller than 30 Å. Pores within porous materials are typically classified as micropores (<20 Å), mesopores (20-500 Å) and macropores (>500 Å), in accordance with the classification adopted by the

IUPAC [Brunauer et al., 1938]. Figure 10 shows fairly homogeneous microporous size distributions. The pore volumes decreased with increasing amount of copper, as the copper particles blocked or were located on the pore walls. Detailed results on the textural properties of the samples are summarized in Table 1. The specific areas, average pore diameters, total and micropore volumes decreased with increasing deposition time. As summarized in Figure 11, the steady-state NO removal efficiency at all temperature was nearly zero (adsorption \approx desorption) when pristine ACF were used. The NO removal efficiency increased with increasing amount of copper to Cu/ACF \approx 110 mg/g due to the increased catalytic reaction. However, the NO removal efficiency decreased for Cu/ACF beyond 110 mg/g, as a result of the decreased adsorption due to the increased amount of copper, even though the catalytic reaction was enhanced.

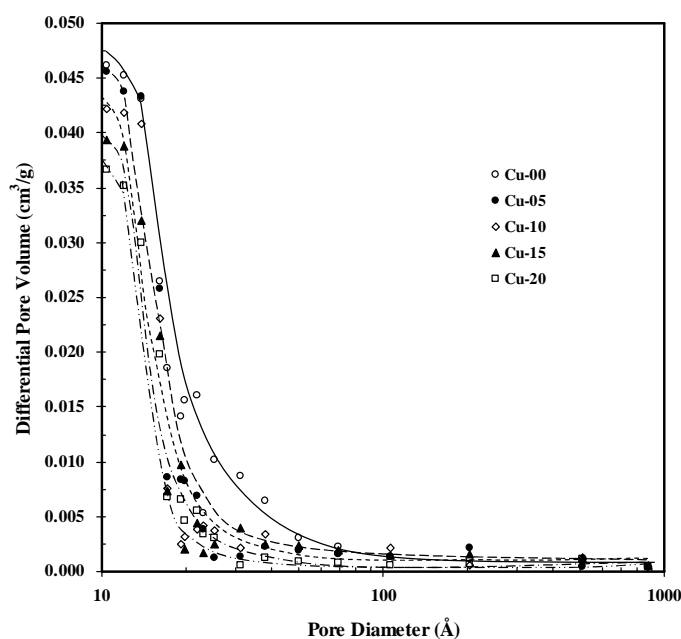


Figure 10. Pore size distributions of the pristine and copper-deposited ACF.

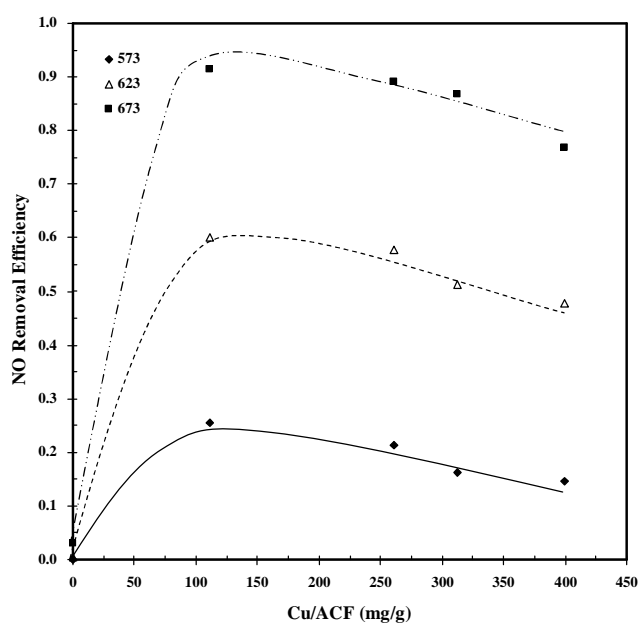


Figure 11. Steady-state NO removal vs amount of copper.

Table 1 Textural properties of the pristine and copper-deposited ACF

Sample	TSSA	TPV	MPV	APD
Cu-00	1,590	0.87	0.77	11.6
Cu-05	1,321	0.72	0.68	10.9
Cu-10	1,201	0.66	0.61	10.6
Cu-15	1,134	0.62	0.57	10.7
Cu-20	1,029	0.56	0.53	10.5

* TSSA: Total specific surface area (m^2/g)

* TPV: Total pore volume (cm^3/g)

* MPV: Micropore volume (cm^3/g)

* APD: Average pore diameter (\AA)

1.3.2 ELDs of Cu and Ag onto rayon-based ACF and applications for antibacterial action and VOC adsorption-desorption

Figure 12 shows the FESEM micrographs of the prepared ACF samples. The particles were found to be copper particles as determined by EDX analyses (see the [Supplementary Data 1](#)). Copper particles having a “snowflake” shape or aggregates of 50 nm-1 μ m are displayed in the copper deposited ACF sample. Figure 12 also shows the results of ICP-AES analyses. Cu-10, Cu-20, and Cu-30 represent the samples obtained at deposition times of 10, 20, and 30 minutes, respectively. As the deposition time increased, there were more particles on the surface of the fiber and the particles grew larger (see the [Supplementary Data 1](#)). In Figure 13, the surface structures of the copper particles obtained by the wide-angle XRD method show that the sharp peaks found at approximately $2\theta = 43^\circ$, 50° , and 74° correspond to the [111], [200], and [220] planes of the copper (JCPDS 4-836) on the ACF surfaces, respectively. The average crystallite sizes, estimated from the XRD line broadening of the [111] peak according to the Scherrer’s equation, were 1.99, 10.37, and 12.98 nm for the copper deposition times of 10, 20, and 30 minutes, respectively. The sharpness of the copper peaks proves that the copper particles are of nearly perfect crystal structure. The intensity of the copper peaks and the crystallinity in the copper deposited ACF were strengthened with increased deposition time.

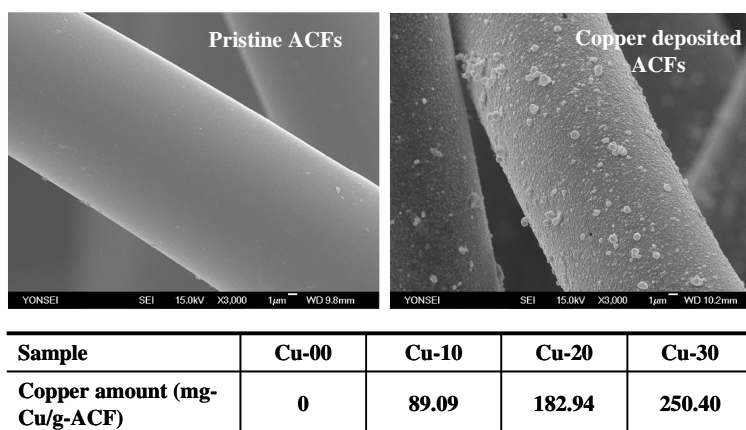


Figure 12. SEM and ICP-AES results of the pristine and copper deposited ACF.

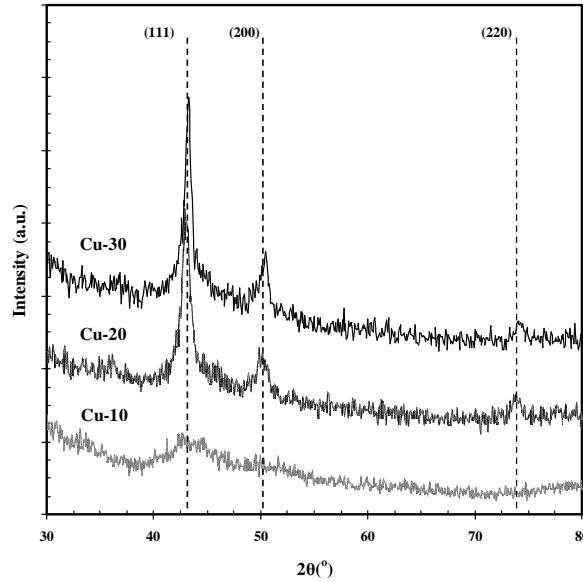


Figure 13. X-ray diffraction patterns of the copper deposited ACF.

- Copper deposited ACF

Antibacterial tests were conducted once the copper particles were characterized. Figure 14 shows the images of the inhibition zones for *B.subtilis*, which were formed in the areas surrounding the prepared ACF samples. The inhibition zone is defined as the area where the bacteria can no longer diffuse towards the sample. The size of bacterial colonies grown on a plate with copper deposited ACF was significantly reduced. The diameters of the inhibition zones of four bacterial strains are also summarized in Figure 14. For any bacterial strain, this diameter is proportional to the copper deposition time. While *E.coli* and *P.fluorescens* (Gram negative) were less susceptible to the action of the samples, Gram-positive bacteria such as *B.subtilis* and *M.luteus* were highly responsive to the amount of copper that was deposited on the ACF sample. One possible explanation for the lower sensitivities of the two Gram-negative

bacterial strains is that the outer membrane of Gram-negative bacteria consists mainly of tightly packed lipopolysaccharide (LPS) molecules, which effectively resist against fine copper particles [Sondi & Salopek-Sondi, 2004; Yoon et al., 2007].

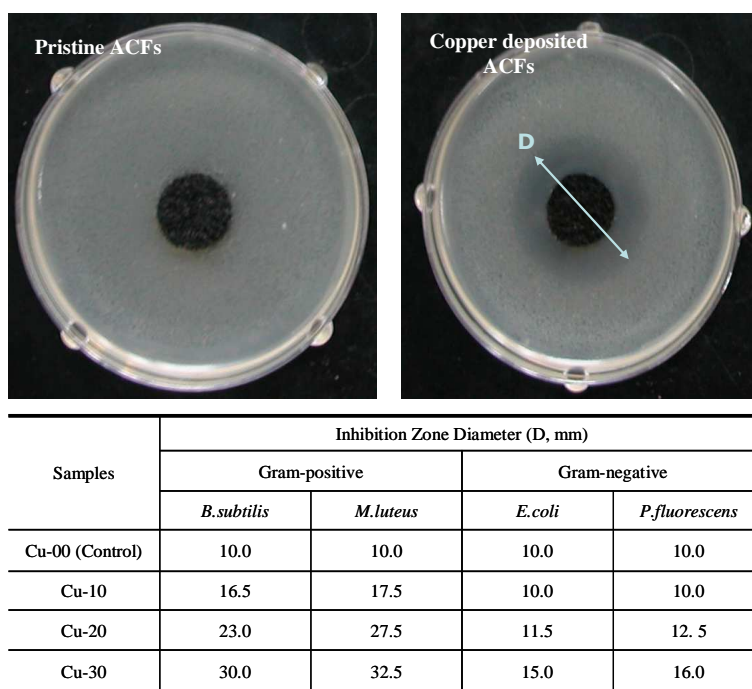


Figure 14. Results for antibacterial tests.

After the stability of copper particles deposited on the ACF samples was checked (see the [Supplementary Data 1](#)), experiments on the adsorption and desorption of VOC were conducted. For adsorption tests, the inlet concentration of VOC was kept constant at 1ppmv. After obtaining a complete breakthrough for adsorption, desorption tests were then performed in the absence of VOC gas injection. In all the test runs, the weight and face velocity of each ACF sample was 750 ± 50 mg (pristine ACF) and 0.5 m/sec, respectively. The VOC concentration profiles of each test were recorded for duration of 400 minutes. Figure 15

describes the breakthrough curves during adsorption and desorption for four different ACF samples. For the adsorption of Cu-00, the breakthrough was almost zero (complete adsorption) until 70 minutes. After it rose sharply at about 80min, then it became unity (zero adsorption) at 250 minutes. The tailing effect was more significant as the copper deposition time increased, due to the blockage of micropores by copper particles in the ACF. The results for desorption tests can be explained similarly. The amounts and effective diffusivities of VOC adsorption and desorption and textural properties of the ACF samples are expressed in the [Supplementary Data 1](#).

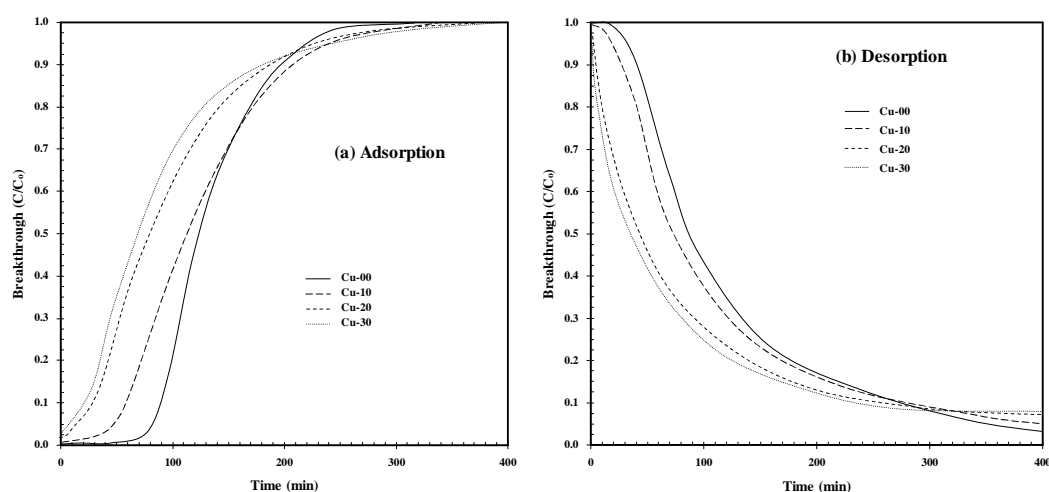


Figure 15. VOC adsorption and desorption characteristics of the pristine and the copper deposited ACF.

- Silver deposited ACF

SEM images of the pristine and silver-deposited ACF discs are shown in Figure 16. The results showed that the pristine ACF disc (Ag-00) had a smooth surface; whereas, the silver-deposited ACF discs had rough surfaces due to the coating of silver particles. In the case of Ag-10, silver particles of about 1 μm were formed, but those on the surface of Ag-20 were

denser and silver completely covered the surface of Ag-30. The total amounts of silver on the ACF filters were measured using ICP-AES analysis and mean crystal sizes were determined according to Scherrer equation using the results of the XRD analysis. The ICP-AES and XRD results are summarized in Table 2. The amounts and mean crystal sizes of silver particles increased from 8 to 35 $\mu\text{g/g}$ and from 12.13 to 15.52 nm, respectively, with the increasing deposition time from 10 to 30 minutes.

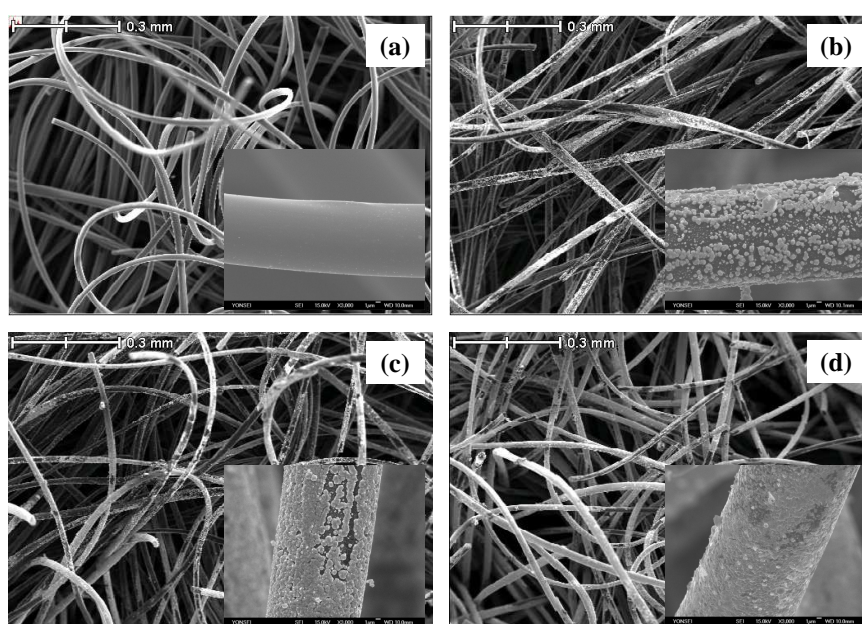


Figure 16. SEM images of (a) Ag-00, (b) Ag-10, (c) Ag-20 and (d) Ag-30.

Table 2 Amounts and crystal sizes of the silver particles deposited onto three ACF discs

	Ag-10	Ag-20	Ag-30
Amount of silver ($\mu\text{g/g}$) ^a	8	28	35
Mean crystal size of silver (nm) ^b	12.13	13.17	15.52

^a Results of the ICP-AES analysis

^b Results of the XRD analysis and Scherrer equation

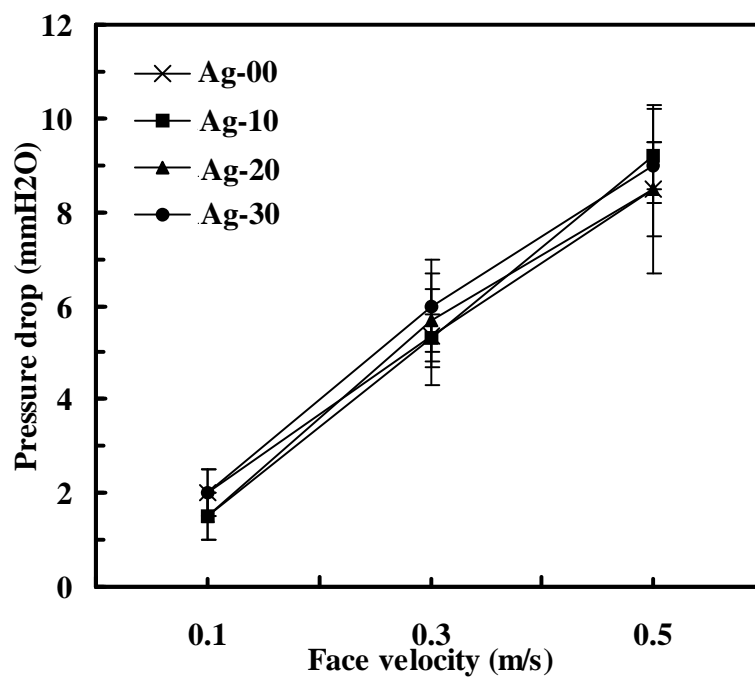


Figure 17. Pressure drop of the ACF filters (Mean \pm SD).

Table 3 shows a summary of the properties related to the adsorptive characteristics of ACF discs which were determined from the raw data of the nitrogen adsorption isotherms according to the BET and BJH methods. The TSSA, micropore specific surface areas (MSSA), TPV, MPV and APD of the silver deposited ACF discs decreased with increasing deposition time. This phenomenon was caused by blockage of the micropores of the ACF by the deposited silver particles. Since decreases in these properties implies a possible loss of active sites for adsorption by the ACF discs, the silver contents supplied for antimicrobial purposes needs to be optimized.

Table 3 Adsorptive properties of the silver deposited ACF discs

	TSSA	MSSA	TPV	MPV	APD
	(m ² /g)	(m ² /g)	(cm ³ /g)	(cm ³ /g)	(Å)
Ag-00	1598	1583	0.91	0.86	17.7
Ag-10	1441	1362	0.60	0.55	16.6
Ag-20	1383	1347	0.58	0.55	17.0
Ag-30	1341	1280	0.55	0.51	16.5

The pressure drops across the filters were measured and as shown in Figure 17, the deposition time did not affect the pressure drop. Figure 17 also shows that the increases in the face velocity, from 0.1 to 0.5 m/s, caused an increased pressure drop from 2 to 9 mmH₂O. The filtration efficiencies of the ACF discs were calculated using the number concentrations measured at upstream and downstream of the filters, using an APS, with the results shown in Figure 18. The size distribution of test bioaerosols generated by the nebulizer is also shown in Figure 18. The aerodynamic mode diameter of the test bioaerosols was 0.78 µm. The size range from 0.67 to 0.89 µm, where the bioaerosols of more than 50 % of total number concentration were found, was used to calculate the filtration efficiency. Regardless of the deposition time, the filtration efficiency was about 0.8 at a face velocity of 0.1 m/s, which decreased to about 0.6 at 0.5 m/s.

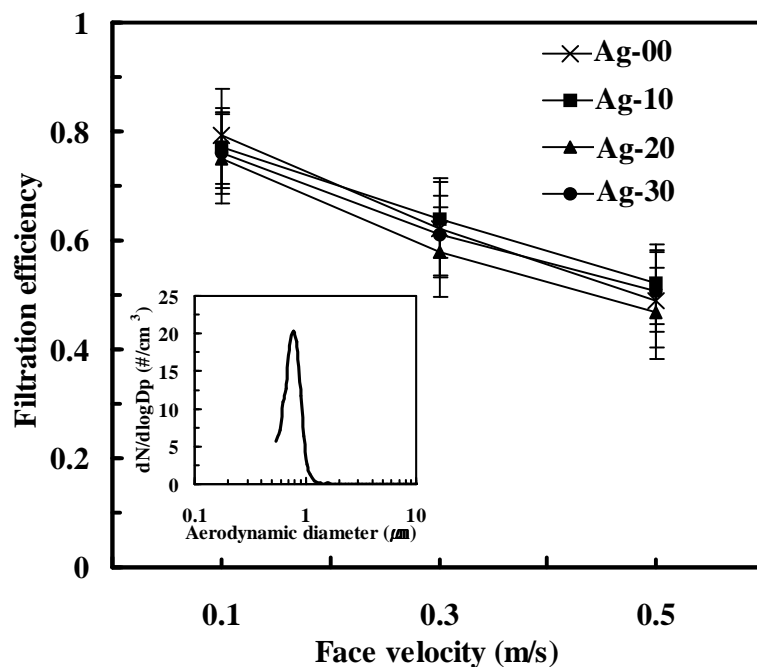


Figure 18. Filtration efficiency of the ACF discs (Mean \pm SD).

The results shown in Figures 17 and 18 indicate the amounts of silver particles were insufficient to cause the variations in the pressure drop or filtration efficiency. The masses of silver particles deposited on the ACF discs were measured using a microbalance (Ohaus, USA): 2.2, 7.6, and 9.5 mg/m² for Ag-10, Ag-20, and Ag-30, respectively. According to Thomas et al. (2001), significant changes in the pressure drop of fibrous filters due to particle deposition occur in the order of g/m² of particle deposition.

The antimicrobial effects of the silver deposited ACF discs were characterized using the disc-diffusion method and the results are represented by inhibition zone diameters in Table 4. For both bacteria, the diameters of inhibition zones increased with increasing deposition

time. For the silver-deposited ACF discs, the bacteria did not grow within or around the filters, while the bacteria did grow on the pristine ACF disc. The test filters with silver particles were considered to release the active forms of silver, for instance, silver ions, which impart antimicrobial activity under humid environment [Melaiye et al., 2005]. The greater numbers of silver particles on the ACF disc, the greater the amount of silver ions would be expected to diffuse further from the filter, due to the larger silver concentration gradient.

Table 4 Diameters of the inhibition zones of the silver deposited ACF discs (Mean \pm SD)

Materials	Diameters of inhibition zones (mm)	
	<i>E. coli</i>	<i>B. subtilis</i>
Ag-00	0	0
Ag-10	10.85 \pm 0.20	11.95 \pm 0.21
Ag-20	11.25 \pm 0.21	13.7 \pm 0.85
Ag-30	11.8 \pm 0.28	14.55 \pm 0.64

The diameters of the inhibition zones of *B. subtilis* were larger than those of *E. coli*. Therefore, silver had better antimicrobial effects against *B. subtilis*, Gram-positive bacteria than against *E. coli*, Gram-negative, as discussed in previous studies [Cho et al., 2005; Yoon et al., 2007]. The lower sensitivities of Gram-negative bacterial strains could probably be explained by the biochemical and physiological characteristics of those bacteria. It is well known that the outer membrane of Gram-negative bacteria is predominantly constructed from tightly packed LPS molecules, which provide an effective resistibility barrier [Brayner et al., 2006; Fan et al., 2002; Papo & Shai, 2005; Sondi & Salopek-Sondi, 2004].

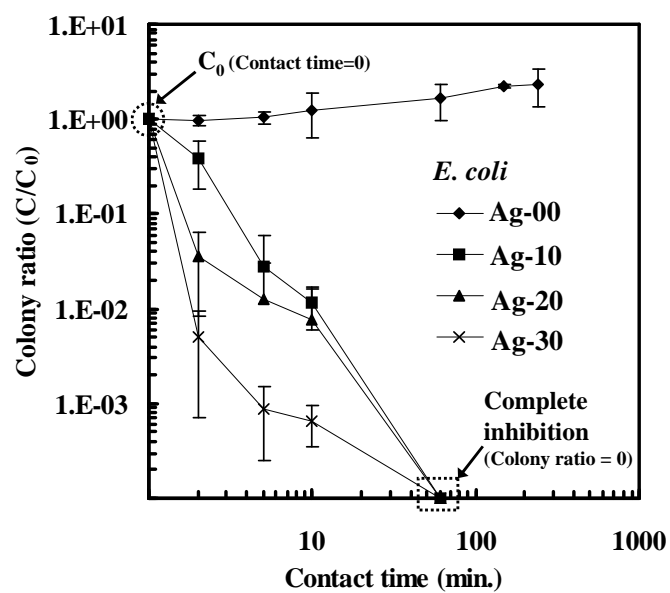


Figure 19. Antimicrobial effects of the test discs on *E. coli* (Mean \pm SD).

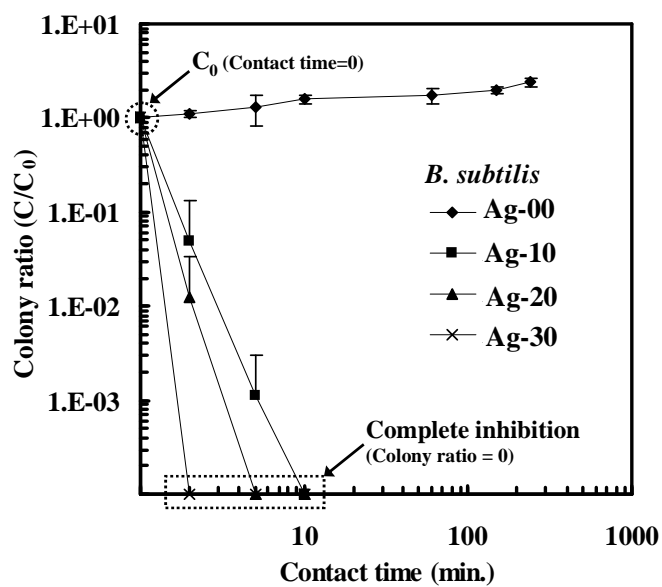


Figure 20. Antimicrobial effects of the test discs on *B. subtilis* (Mean \pm SD).

Figures 19 and 20 show the temporal variations in the colony ratio (C/C_0) of *E. coli* and *B. subtilis* on the tested ACF discs over a 240 minutes period, respectively. On the pristine ACF, the colony ratio of both bacteria increased with time implying breeding of bacteria on the pristine ACF discs. As the contact time or amount of silver increased, the colony ratio decreased, as shown in both Figures. While, *E. coli* was completely inhibited for all silver containing ACF discs after 60 minutes, the colony ratio of *B. subtilis* decreased more rapidly due to lower resistivity of *B. subtilis* against silver, as discussed in the disc-diffusion experiments.

1.3.3 Progresses of Cu and Ag ELDs onto MWNT

Figure 21(a) shows a HRTEM image of the acid-treated MWNTs. Cracks in the image were generated on the MWNTs due to acid attack (see arrows). Figure 21(b) shows a HRTEM image of the MWNTs after they had been activated and accelerated. Palladium particles (seen as tiny black spots in Figure 21(b)) were not distributed densely over the tube-surfaces but were localized at various points along the tube, as discussed by [Ang et al. \(1999\)](#). These catalytic Pd particles were mainly 0.8 nm in diameter while particles larger than 0.8 nm were detected occasionally. Figure 21(c) shows a HRTEM image of the MWNTs after silver ELD for 3 minutes. At this stage, silver nanoparticles, which appear as regions of darker contrast in the image, were deposited selectively on the interior surfaces of the MWNTs due to the presence of concentrated chemical species, such as functional groups, Sn-Pd catalysts, silver ions and reductants on the interior surfaces. Capillary suction [[Ajayan & Iijima, 1993](#); [Ugarte et al., 1996](#)] might help concentrate the chemical species onto the interior surfaces of the MWNTs. At the acid-treatment step, the interior surfaces of the MWNTs might be effectively

attacked by the acid allowing the formation of functional groups on the interior surfaces. In the subsequent Sn-Pd activation step, colloidal Sn-Pd species were also induced on the interior surfaces by capillary suction and then attached to the functional groups by adsorption [Satishkumar et al., 1996]. When the ELD time was 5 minutes, silver particles were deposited in both the interior and exterior surfaces of the MWNTs, as shown in Figure 21(d). When the ELD time was extended to 10 minutes (Figure 21(e)), the silver deposition layer grew laterally and vertically, completely covering the MWNTs. For ELD of 5 and 10 minutes, the mean diameter of the MWNTs was ~85 nm and ~105 nm, respectively. A closer examination of morphology of silver nanoparticles on the exterior surface of the MWNT (inset of Figure 21(f)) revealed them to be agglomerates. According to image analyses, Figure 21(f) shows that the average diameter of the silver particles after ELD for 3, 5, and 10 minutes was 1.3, 1.9, and 2.6 nm, respectively. Figure 21(g) shows the EDX profile for the silver deposited MWNTs corresponding to Figure 21(d). The profile shows peaks for silver along with peaks for C and Fe. The Fe originated from commercial MWNTs because Fe had been used as the catalyst to synthesize the MWNTs. The observed oxygen peak might have originated from the pre-treatment of the MWNTs before silver ELD. Tin peaks were also detected in the profile, which might have been due to the Sn-Pd activation process. Although palladium was not detected by EDX, inductively coupled plasma atomic emission spectroscopy (ICP-AES) analyses indicated a palladium concentration of approximately 640 ppm, which is below the EDX detection limit. The silver-to-carbon fraction increased from 7.00 to 28.20% in mass (1.37 to 5.98% in atom) when the ELD time was increased from 3 to 10 minutes.

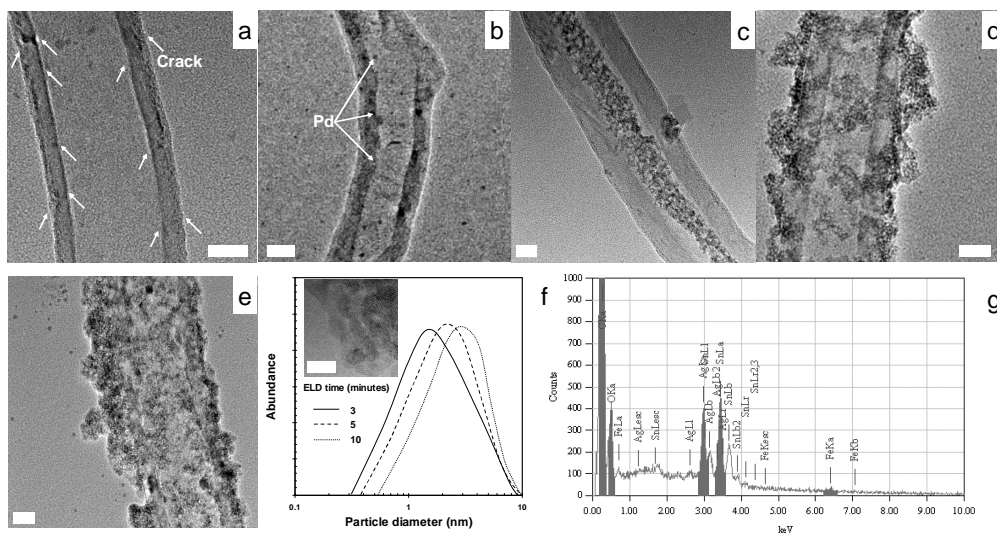


Figure 21. Morphological and chemical analyses of the MWNTs. (a) HRTEM image (scale bar, 20 nm) of the nitric acid-treated MWNTs. (b) HRTEM image (scale bar, 20 nm) of the Sn-Pd activated and accelerated MWNTs. (c) HRTEM image (scale bar, 20 nm) of the silver coated MWNTs (for 3 minutes). (d) HRTEM image (scale bar, 20 nm) of the silver coated MWNTs (for 5 minutes). (e) HRTEM image (scale bar, 20 nm) of the silver coated MWNTs (for 10 minutes). (f) Particle size distribution of silver particles on the MWNTs from the HRTEM image (scale bar, 5 nm). (g) EDX profile of the silver deposited MWNTs (for 5 minutes).

Figure 22 shows the XRD patterns highlighting the major diffraction peaks of the silver particles. All XRD peaks were indexed to the silver face-centered-cubic (fcc) phase based on the JCPDS data. The peaks at 38.2° , 44.3° , 64.5° , and 77.4° (2θ) were assigned to the [111], [200], [220], and [311] planes of the fcc phase of silver. The peak intensities increased with increasing ELD time, which suggests that the metallic silver area increased with

increasing ELD time. The average crystal sizes of the silver particles calculated using the Scherrer formula were 0.9, 1.1, and 1.8 nm for an ELD time of 3, 5, and 10 minutes, respectively. The calculated sizes were smaller than those obtained from the HRTEM observations (1.3, 1.9, and 2.6 nm for 3, 5, and 10 minutes of ELD, respectively). These differences might be due to interference from the MWNTs during XRD analyses.

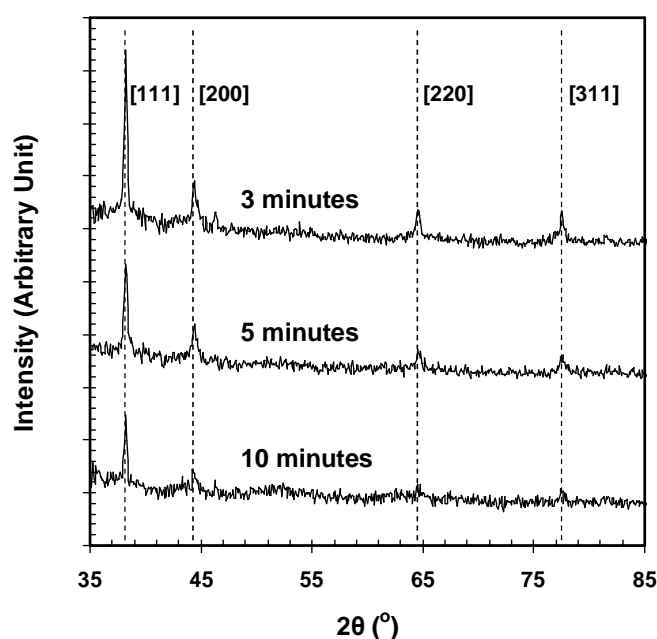


Figure 22. XRD patterns of the silver coated MWNTs.

Figure 23 shows the nitrogen adsorption isotherms of MWNTs at 77K. The sharp increase in each curve from $P/P_0 = 0$ to 0.05 was attributed to rapid adsorption in the micropores of the MWNTs. The curve increased slowly from $P/P_0 = 0.05$ to 0.85 due to capillary suction at the site of the mesopores [Chen et al., 2007]. Figure 23 also shows a sharp

increase in P/P_0 ranging from 0.9 to 0.99 due to strong capillary condensation. All samples exhibited a type II adsorption isotherm according to the IUPAC classification, as reported by Rodriguez [Rodriguez, 1993].

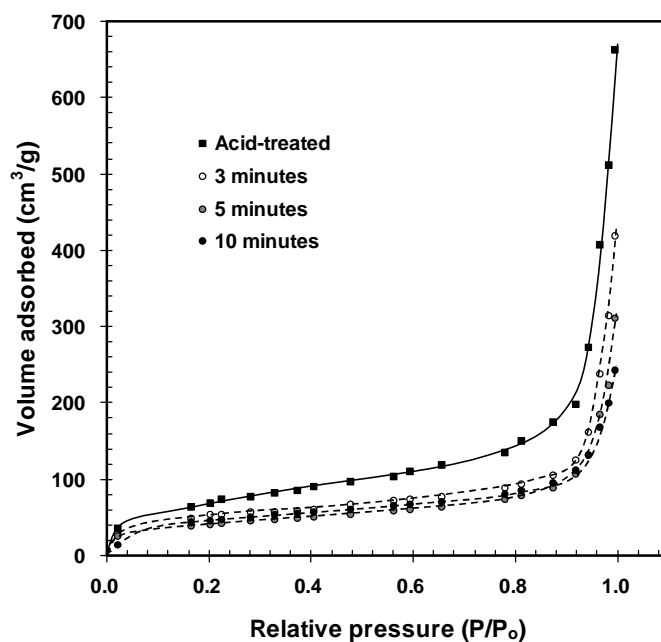


Figure 23. Adsorption isotherms of the silver coated MWNTs.

The amount of nitrogen adsorbed was inversely proportional to the ELD time. This might be due to the blockage of pores in the MWNTs by silver particles. Accordingly, the total BET surface areas for the acid-treated MWNTs and the MWNT reacted with ELD for 3, 5, and 10 minutes were 261.07, 193.65, 162.73, and 143.58 m^2/g , respectively. The total pore volume for the acid-treated MWNTs and the MWNT reacted with ELD for 3, 5, and 10 minutes was 1.022, 0.676, 0.479, and 0.376 cm^3/g , respectively. Table 5 also shows the surface

areas and volumes of the micro and mesopores, and the mean pore diameter. The results suggest that an ELD of 3 minutes causes a large decrease in porosity with most of the adsorptive sites being occupied within 3 minutes.

Items Samples	Total		Microporous		Mesoporous		APD ^c (Å)
	SA ^a (m ² /g)	PV ^b (cm ³ /g)	SA (m ² /g)	PV (cm ³ /g)	SA (m ² /g)	PV (cm ³ /g)	
Acid-treated	261.07	1.022	61.38	0.164	199.69	0.858	194.46
3 minutes	193.65	0.676	43.52	0.117	150.13	0.559	172.68
5 minutes	162.73	0.479	36.57	0.083	126.16	0.396	155.21
10 minutes	143.58	0.376	31.43	0.027	112.15	0.349	110.55

Table 5 Textural properties of the silver coated MWNTs

^a “SA” is the surface area, ^b “PV” is the pore volume, and ^c “APD” is the average pore diameter.

Experiments were also carried out using copper ([Supplementary Data 2](#)). For copper ELD, the progress of metallization of the MWNTs was similar to that of silver ELD. However, when thin-MWNTs (< 5 nm in inner diameter) were used, there was no metallization at the interior surfaces of the thin-MWNTs observed because the capillarity decreases with decreasing tube diameter, as reported by [Ugarte et al. \(1996\)](#) who suggested that the capillarity depends on the inner diameter of the MWNTs and that the nanotube-liquid interface energy decreases with decreasing inner diameter.

1.4 Summaries and conclusions

With the metal particles-deposited on the ACF, the removal of NO and antibacterial action including adsorption-desorption of VOC for different deposition times ranging from 5 to 30 minutes were tested. For NO removal, experiments on the removal of NO in the absence of oxygen were carried out in a packed bed tubular reactor with various reaction temperatures ranging between 423 and 673 K. For all deposition times, the efficiency increased with increasing reaction temperature up to 673 K. The efficiency increased as the amount of copper increased to Cu/ACF \approx 110 mg/g due to the increased catalytic reaction. However, the efficiency decreased above Cu/ACF \approx 110 mg/g because of the decreased adsorption of NO as a result of the increased amount of copper, even with the increased catalytic reaction.

For antibacterial action, the diameters of the inhibition zone of the bacterial colonization were measured and found to be proportional to the copper deposition time. For VOC adsorption and desorption, the results showed that the complete breakthrough time increased with the increasing copper nanoparticles deposition time, but the amounts and diffusivities of VOC adsorption and desorption decreased. This was due to the blockage of micropores by the copper particles, as was seen by BET analyses. An optimum amount of copper needs to be deposited on the ACF for efficient VOC adsorption and desorption.

Silver particles were coated onto an ACF filter, using an electroless deposition method and their efficacy for bioaerosols removal was tested. The results showed that the silver-deposited ACF filters were effective for the removal of bioaerosols by inhibiting survival of microorganisms; whereas pristine ACF filters were not. Two bacteria, *B. subtilis* and *E. coli*, were completely inhibited within 10 and 60 minutes, respectively. ELD of silver did not influence the physical characteristics of ACF filters such as pressure drop and filtration efficiency.

The progress of silver metallization on MWNTs during electroless deposition was examined for a deposition time ranging from 3 to 10 minutes. The results show that the metallization of face-centered cubic silver on the MWNTs progressed from the interior surfaces of the MWNTs to the exterior surfaces. The percentage silver in the coated MWNTs increased from 7.0 to 28.2% by weight. The crystallite size increased from 1.3 to 2.6 nm. However, the surface area and pore volume decreased from 261 to 144 m²/g and from 1.02 to 0.38 cm³/g, respectively.